The Astrophysical Journal, 671:1820–1831, 2007 December 20

THE NATURE OF THE DENSE CORE POPULATION IN THE PIPE NEBULA: CORE AND CLOUD KINEMATICS FROM $C^{18}O$ OBSERVATIONS

August A. Muench,[1] Charles J. Lada,[1] Jill M. Rathborne,[1] João F. Alves,[2] and M. Lombardi[3,4]
Received 2007 June 11; accepted 2007 September 4

ABSTRACT

We present molecular line observations of 94 dark cloud cores identified in the Pipe nebula through near-IR extinction mapping. Using the Arizona Radio Observatory 12 m telescope, we obtained spectra of these cores in the $J = 1–0$ transition of $C^{18}O$. We used the measured core parameters, T_R^*, Δv, v_{lsr}, radius, and mass, to explore the internal kinematics of the cores, as well as their radial motions through the larger molecular cloud. We find that the vast majority of the dark extinction cores are true cloud cores, rather than the superposition of unrelated filaments. While we identify no significant correlations between the cores' internal gas motions and their other physical parameters, we identify spatially correlated radial velocity variations that outline two main kinematic components of the cloud. The largest is a 15 pc long filament that is surprisingly narrow both in spatial dimensions and in radial velocity. Beginning in the "Stem" of the Pipe, this filament displays uniformly small $C^{18}O$ line widths ($\Delta v \sim 0.4$ km s^{-1}), as well as core-to-core motions only slightly in excess of the gas sound speed. The second component outlines what appears to be part of a large (2 pc; $10^3 M_\odot$) ringlike structure. Cores associated with this component display both larger line widths and core-to-core motions than cores in the main cloud. The Pipe molecular ring may represent a primordial structure related to the formation of this cloud.

Subject headings: dust, extinction — infrared: ISM — ISM: clouds — ISM: kinematics and dynamics — stars: formation

1. INTRODUCTION

The Pipe nebula is a nearby (130 pc), large (15 pc) dark molecular cloud lying in projection against the Galactic bulge ($l \sim 0^\circ, b \sim 5^\circ$) and visible to the unaided eye. In addition to being one of the nearest dark clouds, it is unique for its apparent lack of star formation. Comparing large-scale CO maps to *IRAS* point sources, Onishi et al. (1999) found only a single site of star formation (Barnard 59; Reipurth et al. 1996; Brooke et al. 2007), although their observations also revealed numerous dense ($C^{18}O$) cores of gas. Given this lack of star formation, the Pipe nebula represents a good target for improving our understanding of the formation and early evolution of dark clouds, before the star formation process has confused or significantly modified a cloud's internal structure or kinematics. Indeed, the Pipe cloud probably lies at the threshold before star formation begins, and its internal structure and kinematics represent the initial conditions of star formation needed to guide theoretical models.

The physical structure of a dark cloud is best revealed through measurements of the dust, and in particular through the mapping of the extinguishing of the starlight of background stars by this dust (Wolf 1923; Lada et al. 1994; Cambrésy 1999; Alves et al. 2001; Dobashi et al. 2005). Lombardi et al. (2006) used a multiband near-IR technique (NICER; Lombardi & Alves 2001) to create a detailed extinction map of the Pipe nebula at a resolution of $\sim 1'$. Filamentary structures with column densities as low as $A_V \sim 1$ mag can be seen weaving through the Pipe, and this extinction map has a spatial resolution and a density contrast ideal for investigating primordial cloud structure. Alves et al. (2007) combined a wavelet analysis of the cloud with a clump-finding routine to identify 159 significant column density enhancements that we will term dark extinction "cores." This terminology follows the literature usage of identifying dark regions of optical extinction (e.g., Lee & Myers 1999) or dust continuum peaks (e.g., Motte et al. 1998) as the cores of molecular clouds. We note that there is no consensus on the defining characteristics of a cloud core; some researchers in the field suggest that the terminology of a "core" should be applied only to those objects that are gravitationally bound. For this work, we retain the use of the term "core," while also noting that such a determination cannot be made from dust absorption measurements alone.

Molecular line observations are important to confirm that extinction cores are dense coherent kinematic structures, and not a random superposition of cloud features such as filaments or multiple cloud cores. Molecular line observations trace both "microscopic" internal motions such as turbulence, infall, rotation, and expansion, and any "macroscopic" bulk mass motions of the dark cores through the large ($10^4 M_\odot$) cloud. Thus, gas tracers are very useful for extracting the kinematics of dark clouds. Here we use molecular gas tracers to explore the kinematic state of the Pipe extinction cores identified in Alves et al. (2007). Specifically, we use observations of $C^{18}O$ at 3 mm to measure the extinction cores' nonthermal internal motions, as well as their ballistic motion through the ambient cloud traced by their radial velocity. This paper is the first in a series exploring the nature of the Pipe extinction cores by integrating tracers of molecular gas at a range of densities, with the structure provided by the extinction map. In Rathborne et al. (2007), we use ammonia observations to explore the densest gas in the cores, deriving kinetic gas temperatures and probing the cores' chemical state. Finally, Lada et al. (2007) provide a synthesis of these results and examine their implications for the ability of these extinction cores to form young stars and, thus, provide an origin for the stellar initial mass function. This paper is organized simply into three subsequent sections.

[1] Smithsonian Astrophysical Observatory, 60 Garden Street, Mail Stop 72, Cambridge, MA 02138; gmuench@cfa.harvard.edu.
[2] Calar Alto Observatory, Centro Astronómico Hispano Alemán, Calle Jesús Durbán Remón 2-2, 04004 Almeria, Spain.
[3] European Southern Observatory, Karl-Schwarzschild-Straße 2, 85748 Garching, Germany.
[4] University of Milan, Department of Physics, Via Celoria 16, 20133 Milan, Italy.

TABLE 1
Observing Log

Observation Date	T_{sys}	N_{obs}
2005		
2005 May 10	270–370	19
2005 May 11	280–360	23
2005 May 12	240–330	36
2005 May 19	340–490	18
2005 Jun 25	490–700	11
2006		
2006 Jan 28	240–280	8
2006 Jan 29	310–430	9
2006 Jan 30	240–440	10
2006 Jan 31	210–290	7
2006 Feb 01	230–270	9
2006 Feb 02	240–290	10

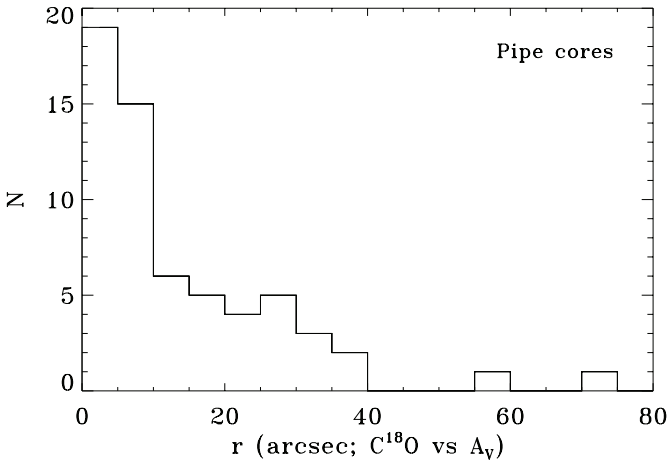

Fig. 1.—Positional offsets (r_{sep}) between the ARO 12 m C^{18}O 56″ beam and the extinction core position reported in Alves et al. (2007). Note that the ARO 12 m C^{18}O beam was centered on the extinction peak of each core.

First, we detail our collection of C^{18}O data for 94 of the 159 Pipe extinction cores identified by Alves et al. (§ 2), finding the vast majority to be coherent cloud structures. In § 3, we analyze the completeness and homogeneity of our data set, and we explore correlations between the extinction cores' structure and internal gas kinematics. Finally, we use our data to examine the large-scale motions of the cores through the Pipe cloud (§ 4), revealing large (10 pc) coherent structures, including a large ring similar to those found in the Taurus star-forming region.

2. DATA

2.1. *Telescope*

Our goal was to survey the molecular gas properties of dark extinction cores identified by Alves et al. (2007) in the 2MASS NICER map of Lombardi et al. (2006). To complete this goal, we used the Arizona Radio Observatory Kitt Peak 12 m telescope (hereafter the ARO 12 m) for 12 nights over a 2 year period (2005–2006). We observed single center pointings of the $J = 1–0$ line of C^{18}O for each core. Table 1 lists the dates of our observations, as well as the typical system temperatures (T_{sys}) and the number of pointings achieved per night; from Tucson, Arizona, the Pipe nebula has a maximum visibility ($\ell > 10^{\circ}$) window less than 5 hr. All observations were performed remotely from Cambridge, Massachusetts.

2.2. *Technique*

We next summarize the observational technique used to obtain the C^{18}O data with the ARO 12 m. Observations were performed using the 3 mm receiver (90–116 GHz) operating in frequency-switching mode with the millimeter autocorrelator. The correlator was configured in dual-polarization mode, with 75 MHz of usable bandwidth in each of two IF banks, having 16,384 channels and an effective spectral resolution of 24.4 KHz per channel, or 0.067 km s^{-1} at 109 GHz. We frequency switched at 5 Hz with a 2 MHz throw; the cloud appears projected against the Galactic bulge, and we did not expect, nor did we observe, any molecular gas not associated with nearby gas clouds (v_{lsr} between 0 and 20 km s^{-1}). Spectral observations at the ARO 12 m use chopper wheel calibration to correct for atmospheric attenuation and telescope losses. This places our data on the T_R^* temperature scale (Kutner & Ulich 1981). The source main beam brightness temperature, T_{mb}, is related to T_R^* by T_R^*/η_m^*, where $\eta_m^* = 0.97$ at 109 GHz at the ARO 12 m, assuming that the source fills the main beam.

The standard observation had an integration time of 10 minutes. For each target, we repeated the standard observation until we achieved an rms noise of <0.1 K per channel; total integrations ranged from 10 to 60 minutes, and this value depended more on the target's elevation than its C^{18}O brightness. All Pipe extinction cores in our sample were detected (at 3 σ or greater) in C^{18}O, with the weakest line having $T_R^* = 0.14$ K (Pipe-100). Individual spectra were summed, folded, baseline subtracted, and Gaussian-profile fit using CLASS. The reduced results assume a rest-frame frequency for C^{18}O $J = 1–0$ of 109,782.173 MHz; this value was determined empirically by Lee et al. (1999, 2001).

2.3. *Targets*

In this section, we describe the targets selected for these observations. The 56″ beam of the ARO 12 m at 109 GHz is well matched to the Gaussian kernel used by Lombardi et al. (2006) to filter spatially individual star extinction estimates derived from the 2MASS point-source catalog. The final 2MASS extinction map has a resolution of 60″ FWHM Gaussian, and was Nyquist sampled to a pixel scale of 30″. In addition, the ARO 12 m beam is much smaller than the 2.7′ beam used by Onishi et al. (1999) to create undersampled C^{18}O maps of ^{13}CO cores (differences in beam size and resolution are discussed in § 3.3.1). Given this optimized beam, we targeted localized peaks of interstellar extinction throughout the Pipe nebula, and assigned priority based initially on maximum column density. We revised our target priorities after the first year's observations to sample lower mass dark cores. In summary, we obtained single pointing C^{18}O data for 94 of the 159 Pipe extinction cores; these targets span the entire range of core masses (0.2–20 $M_{\odot}$; Alves et al. 2007). The completeness and homogeneity of this sample of cores are examined in § 3.

While we targeted the localized extinction peak within each Pipe core, our pointing centers correspond very closely to the core centers reported in Alves et al. (2007),[5] typically lying within a single resolution element of the A_V map. The distribution function of separations between the published core centers and the C^{18}O pointings is given in Figure 1.

[5] The centers for the Pipe extinction cores listed in Alves et al. were derived using a 2D version of Clumpfind (Williams et al. 1994).

TABLE 2
$C^{18}O$ DATA

Pipe (ID)	Flag[a]	R.A. (J2000.0)	decl. (J2000.0)	r_{sep} (arcsec)	v_{lsr} (km s^{-1})	dv (km s^{-1})	T_R^* (K)	rms (K)	ΣA_V[b] (mag)
6		17 10 31.01	−27 25 33.31	8.07	3.501	0.391	2.066	0.06	99.6
7		17 11 36.39	−27 33 50.70	19.97	3.935	0.517	1.366	0.05	85.6
8		17 12 15.04	−27 37 44.41	2.76	3.462	0.390	2.012	0.05	88.7
11		17 10 49.87	−27 23 04.07	6.06	3.446	0.455	1.524	0.07	85.2
13		17 10 47.22	−27 13 41.43	9.64	3.751	0.336	0.498	0.05	39.4
14		17 12 31.40	−27 21 26.02	3.82	3.506	0.407	3.058	0.06	127.1
15		17 12 52.20	−27 23 29.87	2.64	3.591	0.375	2.601	0.08	75.3
16		17 13 14.81	−27 25 45.25	31.95	3.349	0.251	1.240	0.11	51.2
17		17 14 04.72	−27 28 02.65	33.32	3.332	0.487	0.360	0.03	38.8
20		17 15 13.95	−27 33 20.50	60.61	9.144	0.348	1.296	0.21	65.3
21		17 14 55.99	−27 21 31.59	4.85	3.546	0.361	0.761	0.11	49.4
22		17 15 47.79	−27 29 34.63	5.87	3.753	0.378	0.791	0.09	55.6
23		17 16 05.39	−27 30 54.57	2.62	3.642	0.343	1.043	0.06	62.1
25		17 16 22.70	−27 10 15.51	18.40	3.742	0.377	0.475	0.09	49.7
26		17 17 00.81	−27 10 01.52	22.83	2.919	0.359	0.391	0.04	37.1
27		17 17 08.56	−27 01 54.20	4.49	3.180	0.204	0.948	0.09	49.1
30		17 20 58.21	−27 13 32.25	21.67	3.234	0.368	0.351	0.03	40.2
31		17 18 30.79	−26 48 39.96	15.90	3.380	0.615	0.578	0.07	50.5
32		17 21 12.09	−27 11 26.84	25.90	3.139	0.339	0.752	0.03	43.0
33		17 19 40.34	−26 55 38.55	16.35	3.357	0.406	1.959	0.05	80.5
34		17 20 17.69	−26 59 22.48	12.20	3.106	0.298	2.114	0.06	62.8
35		17 22 20.45	−27 14 35.63	20.13	2.926	0.540	0.172	0.03	38.6
37		17 19 33.78	−26 43 45.11	28.30	3.310	0.371	1.493	0.10	64.0
40		17 21 14.63	−26 53 01.38	23.15	3.286	0.380	1.848	0.05	174.1
41		17 22 27.64	−27 04 02.84	13.41	3.747	0.339	1.744	0.06	71.9
42		17 22 40.52	−27 05 04.19	9.83	3.797	0.306	3.193	0.07	150.4
43		17 21 58.97	−26 51 07.23	9.44	3.372	0.351	1.079	0.10	48.8
46		17 24 23.49	−26 32 03.82	35.38	3.090	0.334	0.407	0.05	37.9
47		17 27 26.27	−26 58 23.46	2.02	2.861	0.484	1.479	0.05	75.4
48		17 25 56.04	−26 44 23.72	2.21	3.611	0.326	2.983	0.06	83.0
51	a	17 27 22.81	−26 44 16.14	10.39	3.648	0.372	1.670	0.07	65.5
	b				3.030	0.601	0.563		
52	a	17 28 19.47	−26 44 02.04	1.77	3.577	0.334	0.853	0.04	50.8
	b				3.039	0.890	0.158		
54		17 30 24.12	−26 49 45.74	4.87	5.836	0.308	0.797	0.08	63.5
56		17 28 11.41	−26 24 09.44	8.46	3.613	0.502	1.547	0.05	85.7
57		17 31 03.73	−26 48 08.58	12.68	5.855	1.203	0.211	0.08	58.9
58	a	17 29 41.96	−26 29 16.61	11.15	3.774	0.772	0.298	0.05	50.8
	b				4.947	0.369	0.237		
59		17 30 49.24	−26 38 34.64	3.42	4.744	0.289	0.653	0.10	56.9
61		17 28 35.63	−26 16 47.08	31.72	3.826	0.448	0.575	0.07	67.7
63	2	17 31 34.85	−26 36 41.42	5.68	5.181	0.924	0.458	0.06	66.5
	a				5.444	0.379	0.504		
	b				4.923	0.457	0.442		
64		17 31 28.27	−26 31 41.48	3.07	5.086	0.491	1.411	0.06	80.1
65		17 31 20.68	−26 30 37.91	4.44	4.993	0.573	1.581	0.05	84.3
66		17 31 13.42	−26 29 02.25	12.90	4.909	0.627	1.377	0.05	82.1
67		17 28 41.88	−25 55 58.81	16.07	4.239	0.463	1.462	0.07	62.1
68		17 30 03.85	−26 03 00.02	20.95	4.458	0.398	0.589	0.11	52.4
70		17 29 37.99	−25 54 28.92	5.88	3.915	0.470	1.915	0.06	80.1
73		17 30 27.258	−25 59 28.57	1.39	4.264	0.361	0.531	0.05	56.4
74		17 32 36.32	−26 15 55.25	14.19	4.211	0.335	1.959	0.06	94.4
75		17 33 04.51	−26 11 24.06	27.99	5.140	0.485	0.648	0.07	62.2
79	2	17 33 08.57	−26 01 46.43	12.97	4.682	0.743	0.748	0.07	78.4
	a				4.843	0.481	0.688		
	b				4.421	0.372	0.553		
80		17 33 32.80	−26 01 42.21	13.72	4.693	0.453	1.075	0.07	81.2
81		17 28 36.50	−25 15 41.55	7.98	3.454	0.316	0.360	0.03	38.4
82		17 34 31.06	−26 02 46.66	32.11	6.356	0.500	0.315	0.05	58.4
84		17 34 51.62	−26 01 31.82	5.14	6.303	0.287	1.086	0.07	61.4
86		17 33 27.15	−25 43 44.12	26.04	4.437	0.403	1.446	0.14	86.5
87		17 34 30.38	−25 49 53.16	84.55	4.753	0.525	1.606	0.05	140.5
88		17 33 47.74	−25 43 36.70	39.54	5.470	0.491	0.979	0.12	91.6
89		17 33 28.54	−25 40 47.98	6.68	4.445	0.465	1.497	0.07	101.2

TABLE 2—*Continued*

Pipe (ID)	Flag[a]	R.A. (J2000.0)	decl. (J2000.0)	r_{sep} (arcsec)	v_{lsr} (km s^{-1})	dv (km s^{-1})	T_R^* (K)	rms (K)	ΣA_V[b] (mag)
91		17 32 13.38	−25 25 16.92	20.35	4.195	0.376	1.134	0.05	85.2
92		17 34 04.99	−25 39 49.30	36.68	5.110	0.517	1.953	0.06	109.4
93	a	17 34 47.18	−25 46 29.21	34.42	5.221	0.554	1.530	0.15	126.5
	b				6.483	0.351	0.375		
94		17 34 35.50	−25 43 16.26	2.97	5.305	0.478	1.006	0.06	89.9
95		17 22 58.55	−23 58 03.80	5.53	4.763	0.501	0.541	0.03	38.5
96		17 23 34.99	−24 02 22.61	36.19	4.767	0.660	0.289	0.03	44.7
97	2	17 33 30.95	−25 30 31.25	20.77	4.128	1.000	0.870	0.04	109.8
	a				4.393	0.370	1.052		
	b				3.924	0.305	0.951		
	c				3.401	0.653	0.280		
98		17 34 40.17	−25 40 26.85	6.51	5.347	0.511	1.166	0.07	100.2
99		17 25 02.08	−24 12 57.98	20.10	4.714	0.296	1.466	0.10	56.0
100		17 32 44.405	−25 21 09.07	1.29	3.840	0.709	0.144	0.05	58.9
101		17 22 39.29	−23 49 59.01	12.99	3.342	0.276	1.648	0.12	81.7
102		17 34 20.53	−25 34 04.73	28.50	4.714	0.296	1.466	0.04	141.4
103		17 36 22.844	−25 49 51.72	1.31	2.830	0.313	1.236	0.05	51.8
105		17 25 10.82	−24 08 31.23	4.06	4.549	0.337	1.259	0.04	54.0
106		17 24 58.64	−24 06 50.64	14.12	4.773	0.313	0.973	0.04	54.9
108	2	17 31 31.51	−24 58 51.30	12.57	5.623	1.169	0.394	0.09	56.2
	a				5.863	0.359	0.634		
	b				5.244	0.331	0.487		
109		17 35 44.90	−25 33 02.00	17.87	5.846	0.380	2.420	0.05	132.8
110		17 28 38.67	−24 27 33.60	7.25	6.091	0.590	0.511	0.04	38.1
111		17 34 42.113	−25 20 28.85	1.32	3.595	0.679	0.295	0.04	62.7
112		17 23 48.45	−23 42 55.64	8.35	4.952	0.329	1.348	0.09	64.6
113		17 23 36.61	−23 41 03.62	16.45	4.675	0.368	1.161	0.09	67.3
114		17 23 05.58	−23 33 41.56	13.15	4.980	0.297	0.283	0.03	30.6
115		17 35 06.55	−25 20 57.07	8.18	3.999	0.400	0.625	0.13	70.4
118		17 35 40.31	−25 22 18.62	4.44	3.744	0.983	0.536	0.04	75.7
119		17 30 32.30	−24 35 27.55	4.09	5.245	0.511	0.470	0.10	51.0
120		17 27 17.43	−24 04 34.95	12.42	4.488	0.816	0.353	0.03	50.5
123	a	17 36 22.25	−25 23 04.26	26.51	3.771	0.316	1.282	0.08	77.9
	b				3.022	0.530	0.371		
127		17 36 30.85	−25 18 59.50	6.11	3.602	0.427	0.953	0.07	87.0
128		17 35 18.71	−25 07 55.03	10.19	15.079	1.043	0.338	0.08	58.0
130		17 37 07.28	−25 15 38.50	13.91	3.866	0.526	0.450	0.06	74.7
131		17 38 05.64	−25 17 06.13	8.16	3.511	0.466	1.168	0.09	81.3
132		17 37 50.86	−25 14 51.71	14.49	3.934	0.491	1.658	0.04	85.0
133		17 28 46.93	−23 53 46.54	10.67	3.156	0.418	1.881	0.11	56.0
135		17 38 58.21	−25 07 44.93	5.68	2.930	0.414	1.247	0.07	57.2
137		17 39 28.03	−25 07 13.19	0.69	2.478	0.325	0.975	0.20	52.7
140		17 39 41.74	−25 01 42.33	15.44	3.072	0.401	0.514	0.09	57.9
145		17 36 56.58	−24 19 29.52	27.72	3.155	0.252	0.433	0.04	50.1

NOTE.—Units of right ascension are hours, minutes, and seconds, and declination degrees, arcminutes, and arcseconds.

[a] Flag given to indicate C^{18}O component for each extinction core. Components "a", "b", etc. are ordered by antenna temperature. Where given, Flag = 2, means that all components fit with a single Gaussian.

[b] Total column density expressed in magnitudes of extinction (A_V) measured in a Gaussian-weighted 56″ beam on the NICER 2MASS map of Lombardi et al. (2006) and centered on the position of the C^{18}O observation.

2.4. *Results*

We provide C^{18}O observations for 94 Pipe extinction cores in Table 2. Identifications correspond to the core IDs given by Alves et al. (2007),[6] and are identical to those given in Lada et al. (2007). The table includes the pointing center for each C^{18}O observation and the results of a Gaussian profile fit.

Nine extinction cores (10% of the sample) displayed multi-peaked profiles in C^{18}O; four of these cores consist of two, and in one case three, distinct lines. We record in the table individual Gaussian fits to each component, identifying the stronger (T_R^*) line as the "a" cloud. In four of the nine cases, the lines are sufficiently blended that in addition to multicomponent fits, we also tabulated the fit of a single Gaussian to the double-peaked profile. We further analyze kinematically distinct and overlapping cloud components in § 4.1.

3. ANALYSIS

3.1. *Completeness*

In this section, we examine the completeness as a function of extinction core mass for our sample of 94 cores for which we obtained C^{18}O line measurements. In Figure 2, we compare the

[6] The Alves et al. extinction core identifications and positions can be obtained using the VizieR service http://vizier.cfa.harvard.edu/viz-bin/VizieR/, and have the catalog id of J/A+A/462/L17.

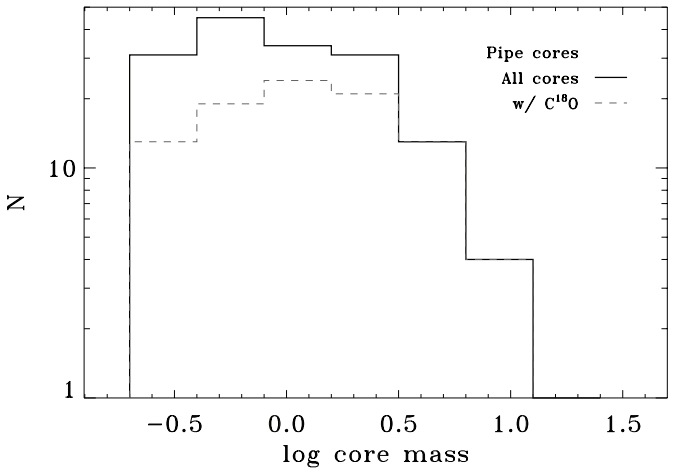

FIG. 2.—Completeness of CO sample. Mass functions for all 159 extinction cores (*solid line*) and for extinction cores with $C^{18}O$ measurements (*dashed line*) are compared. Masses are taken from the wavelet-subtracted map as tabulated in Lada et al. (2007).

mass function of all 159 Pipe cores to the mass function for our sample with $C^{18}O$ data. Note that the masses ($M_{\rm core}$) and radii of the extinction cores used in this paper were derived by and are found in Lada et al. (2007). Briefly, Lada et al. integrated the background-subtracted extinction map of Alves et al. (2007) for cores with positions and sizes determined by the two-dimensional version of Clumpfind (Williams et al. 1994). We list in Table 3 our completeness statistics. Our sample includes 100% of the extinction cores with masses greater than about 3 $M_\odot$, with the sole exception of the star-forming core Barnard 59 (Pipe-12; $M = 20\,M_\odot$). Between 1 and 3 $M_\odot$, our sample is ~70% complete. Below 1 $M_\odot$, our sample includes ~40% of all the Alves et al. Pipe extinction cores.

Our observations of the Pipe extinction cores are spatially nonuniform. We plot in Figure 3*b* the 2MASS/NICER extinction map from Lombardi et al. (2006), segregating cores with and without $C^{18}O$ by color. For the main body of the Pipe (decl. $< -24^\circ 45'$), we achieved a degree of completeness much higher than in the composite core population: >80% for 1–3 $M_\odot$ cores and >70% of the sub-solar-mass cores. In the next section, we explore the spatial homogeneity of the properties of the observed cores.

3.2. *Spatial Homogeneity*

In this section, we evaluate our sample of $C^{18}O$ observed extinction cores, comparing internal subsets of the data that are defined by their location in the cloud. Spatial subsets provide a means to evaluate our somewhat nonuniform spatial coverage; however, our spatial partitioning of the Pipe nebula is further motivated by clear physical properties of the cloud.

In Figure 3*a*, we illustrate the dependence of a core's radial velocity on Galactic longitude. The range of observed $v_{\rm lsr}$, 3-7 km s^{-1}, is consistent with that found for $C^{18}O$ cores throughout Ophiuchus (Tachihara et al. 2000), although we do not observe any core with $v_{\rm lsr} < 2$ km s^{-1}, of which Tachihara et al. observed several.[7] But unlike Ophiuchus, the spatial distribution of $v_{\rm lsr}$ is highly structured, displaying strong correlations with Galactic longitude.

Based on our spatial completeness and these $v_{\rm lsr}$ variations, we divided the Pipe nebula into three regions. Each region was assigned a name that alludes to the morphology of a smoking pipe (see Fig. 3). There is a long (4.2°, 10 pc) straight (aspect ratio, $a/b \sim 3.5$) filament tracing eastward from Barnard 59 [$(l, b) = (357.1^\circ, 7.1^\circ)$], which Barnard et al. (1927) originally called the "Sinkhole." We will refer to this very straight filament as the "Stem" of the Pipe. The Stem displays extremely little variation in $v_{\rm lsr}$ about a mean of 3.5 km s^{-1}. The Stem merges with a large dark "Bowl" at approximately $l = 0^\circ$, which is where $v_{\rm lsr}$ increases by 1.5 km s^{-1}, although there is larger dispersion in $v_{\rm lsr}$ in the Bowl than in the Stem. Above the Bowl (decl. $< -24.75^\circ$), there are widely dispersed smaller clouds, including the dark globules of Barnard 68, 72, and 74. We will call this region the "Smoke"; our $C^{18}O$ sample is most incomplete in the Smoke. For reference, the Smoke of the Pipe connects to an extinction bridge (beyond this map) that extends 10° northward (Dobashi et al. 2005), connecting it to the Ophiuchus main cloud.

[7] Two cores having $v_{\rm lsr} > 7$ km s^{-1}, specifically at 9 and 15 km s^{-1}, do not appear in Fig. 3, and are not further examined in this work.

TABLE 3
$C^{18}O$ CORE COMPLETENESS

	FULL CATALOG			STEM AND BOWL		
log $M_\odot$	$N_{\rm cores}$	$N_{\rm obs}$	% Obs.	$N_{\rm cores}$	$N_{\rm obs}$	% Obs.
−0.550	31	13	42.	17	12	71.
−0.250	45	19	42.	21	16	76.
0.050	34	24	71.	23	20	87.
0.350	31	21	68.	18	15	81.
0.650	13	13	100.	13	13	100.
0.950	4	4	100.	4	4	100.
1.250	1	0	0.	1	0	0.

We used two-sided Kolmogorov-Smirnov (K-S) tests to determine whether these spatial samples could be drawn from the same parent. For these samples, there is a null possibility (10^{-8}) that the $v_{\rm lsr}$ distributions for the Stem and the Bowl are drawn from the same parent. The Smoke's $v_{\rm lsr} \sim 5$ km s^{-1} is very similar to, and probably drawn from, the same parent as the Bowl; the K-S probability for the Bowl and the Smoke is 0.18. Careful inspection of Figure 3*a*, however, reveals that bulk variations in $v_{\rm lsr}$ with position in the cloud are actually more interesting in detail than we have examined here. In particular, the increased dispersion of $v_{\rm lsr}$ in the Bowl is due to systematic motions (§ 4.1), while most of the extinction cores that we found to display multiple $C^{18}O$ components are also found in the Bowl.

We tested the extinction cores' remaining physical parameters (T_R^*, Δv, $M_{\rm core}$) for spatial homogeneity using these subsets. In Figure 4, we plot these three physical core parameters versus Galactic longitude. Note that for simplicity, the figure only segregates the Smoke cores by symbol; Bowl cores are those with $4^\circ > l > 0^\circ$ (and decl. $> -24.75^\circ$). As can be inferred visually from Figure 4*a*, the three Pipe regions cannot be distinguished ($P_{\rm K\text{-}S} \sim 0.3$) by the values of antenna temperature (T_R^*).

The spatial distribution of $C^{18}O$ line widths is shown in Figure 4*b*. While the Smoke cores could have the same parent as those of either the Stem or the Bowl, the Stem and the Bowl have Δv distributions sufficiently different ($P_{\rm K\text{-}S} \sim 0.002$) to warrant closer inspection. Cores with multiple CO components were not used for these tests, although the test results do not change when they are included. The slight differences between the Stem and the Bowl remain even if we remove the two $\Delta v > 0.8$ km s^{-1} cores, which could also represent unresolved double-lined components. To further explore the slight difference in line widths between the Stem and the Bowl, we plot Δv as a function of $v_{\rm lsr}$ in Figure 5. As we have shown that the Stem and the Bowl have distinct, distinguishable $v_{\rm lsr}$ distributions, it is not surprising that the slight differences in Δv for these two regions manifest themselves in

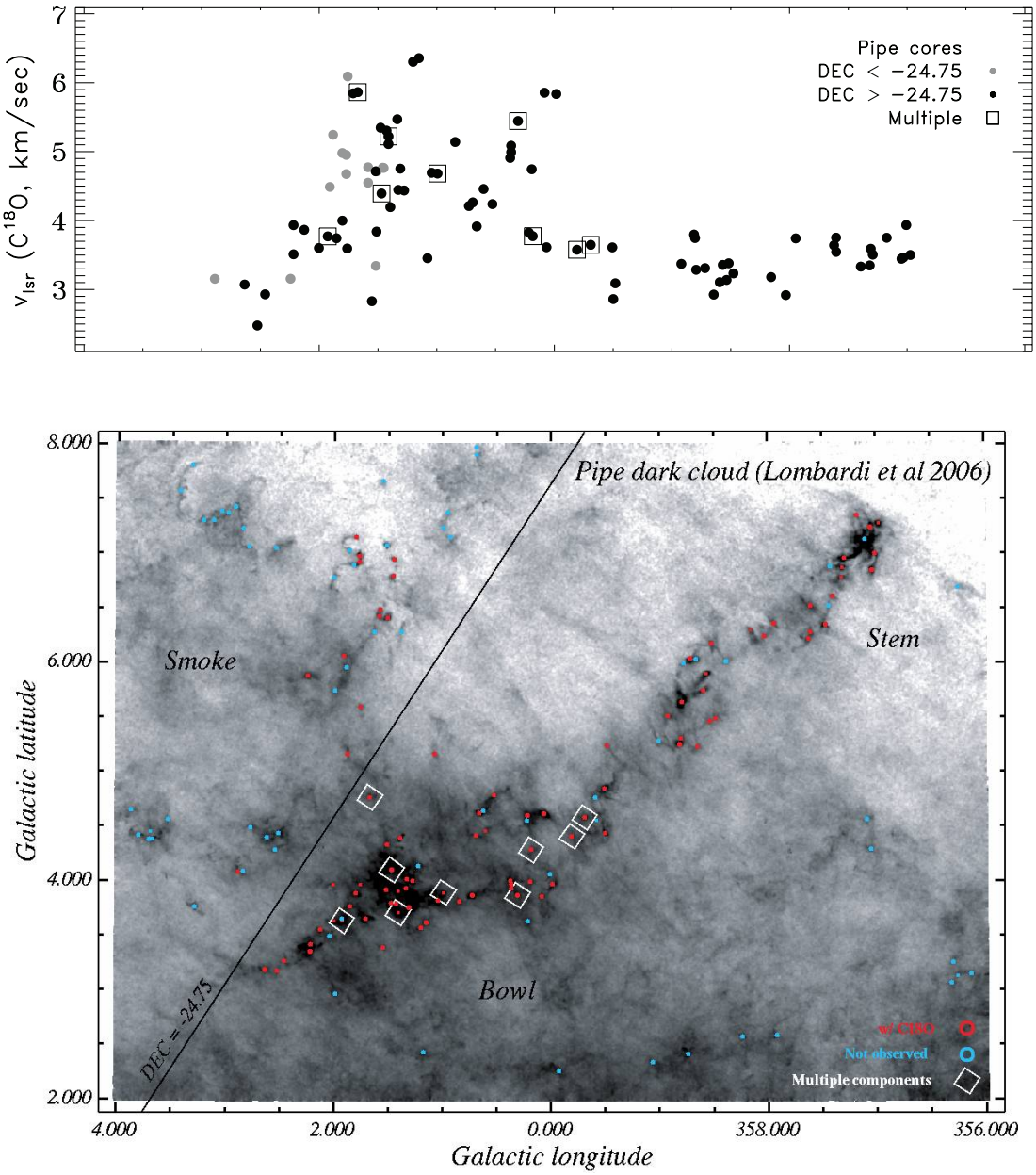

FIG. 3.—Spatial distribution of Pipe extinction cores. *Top*: Spatial variations in v_{lsr} of the Pipe cores observed in C^{18}O. *Bottom*: Spatial distribution of Pipe cores with and without C^{18}O measurements, with underlying reverse gray-scale image of the Pipe nebula in extinction (Lombardi et al. 2006). Three subregions of the Pipe referred to in text (Stem, Bowl, and Smoke) and used to characterize the sample are so labeled. Sources surrounded by diamonds display multiple C^{18}O line components. The bottom figure was created using SAOImage DS9 (Joye & Mandel 2003).

a correlation with v_{lsr}. A linear fit suggests that Δv increases by 0.05 km s^{-1} per unit increase in v_{lsr}. As we will discuss further in § 4.1.2, the larger line widths within the Bowl are related to an interesting large-scale kinematic feature of the Pipe nebula.

Interestingly, the distribution of extinction core masses along the length of the Pipe is consistent with a single parent population: $P_{K\text{-}S} \sim 0.3$ when comparing the Bowl to the Stem. Furthermore, the mass distributions for that sample of cores with C^{18}O in the three regions are also indistinguishable ($P_{K\text{-}S} \sim 0.1$). Moreover, the mass distribution of extinction cores that display multiple C^{18}O components is basically uniform, and we confirm the vast majority of these extinction cores as real, dense cloud structures. Thus, we can conclude that the removal of such multicomponent "cores" from the ensemble core mass function would not change any of the conclusions of Alves et al. (2007). In fact, there is no quantity in our data that is systematically contaminated by extinction cores displaying multiple C^{18}O components.

3.3. *Correlations*

3.3.1. *Core Line Width–Size*

There is no true correlation between the physical size of the Pipe extinction cores and their C^{18}O line width (Fig. 6). A weak negative correlation ($r_c \sim -0.2$) is misleading, because a least-absolute-deviation linear fit, which is robust against the clear outliers in this sample, reveals nothing meaningful. All fits and correlation coefficients are given in Table 4.

As we only sample the line width at the center of each extinction core, it is perhaps meaningful to ask if the C^{18}O line width varies on larger angular scales within the Pipe nebula. While

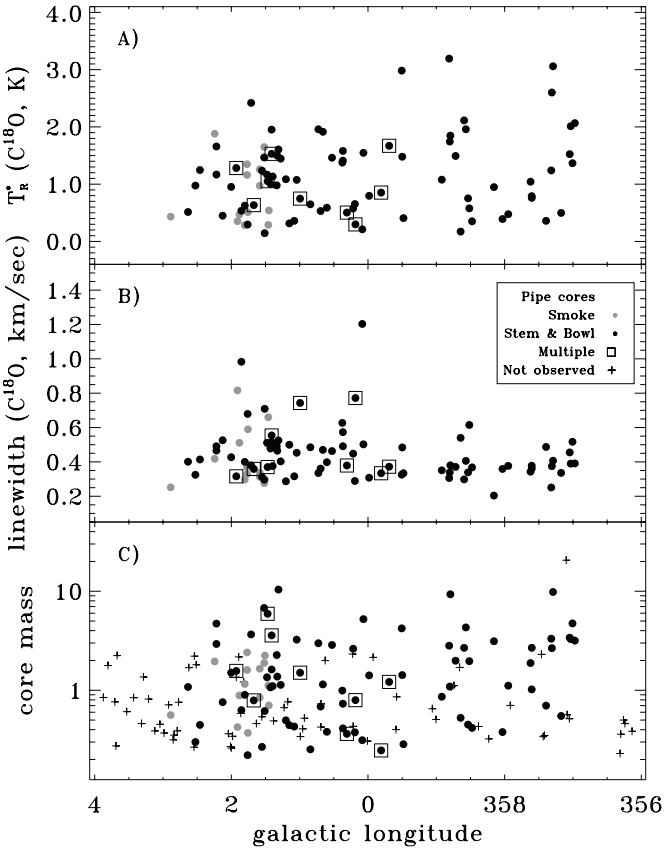

FIG. 4.—Homogeneity of core samples. Core gas and dust measurements as a function of Galactic longitude. For multiple component cores, we plot the profile fit values for the "a" or brighter component.

variations of v_{lsr} on the largest scales of the Pipe are discussed in § 4.1, we can compare our results to the integrated $C^{18}O$ line widths data published by Onishi et al. (1999). These NANTEN data were taken with a beamwidth 3 times larger than the ARO 12 m, and their $C^{18}O$ data correspond only to undersampled maps of ^{13}CO peaks, which miss much of the structure of the Pipe. Indeed, we find that 12 NANTEN $C^{18}O$ cores contain 20 extinction cores. In 8 cases where a single NANTEN core contains only 1–2 extinction cores, we find that an additional line width component on the order of the line width of an individual extinction core is needed to recover the larger scale integrated line width. Determining whether this additional component comes from organized v_{lsr} variations in the gas or from general intercore turbulence requires fully sampled maps. We do note that in a few cases where we have measurements for multiple extinction cores per NANTEN core, v_{lsr} variations between cores within the NANTEN beam are sufficient to explain these differences.

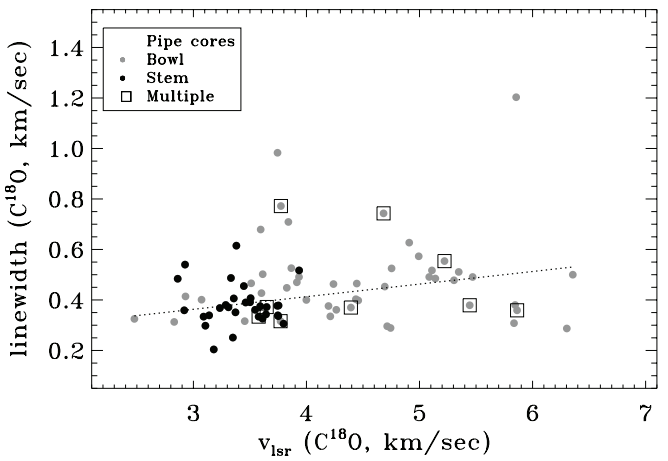

FIG. 5.—Correlation of Δv with v_{lsr}. Symbols segregated by color correspond to cores in the Stem and Bowl of the Pipe. Smoke cores are not included in this plot. Circles surrounded by squares represent the "a" component of extinction cores displaying two $C^{18}O$ components. Note the very small dispersion in the values of both v_{lsr} and Δv in the Stem. A least-absolute-deviation fit is shown (Table 4).

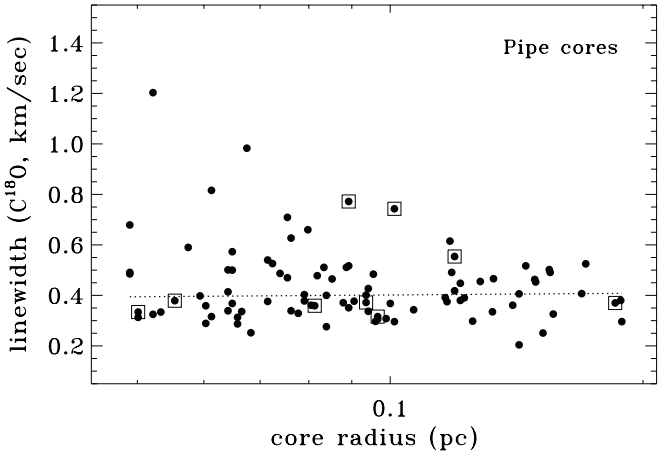

FIG. 6.—Core line width–size relation for Pipe cores. Circles surrounded by squares represent the "a" component of extinction cores displaying two $C^{18}O$ components. A least-absolute-deviation fit is shown (Table 4).

3.3.2. *Core Line Width–Mass*

In this section, we explore the dependence of the $C^{18}O$ line width on the mass of the individual Pipe extinction cores. We use the mass of each Pipe extinction core as derived from the wavelet analysis of the extinction map, which effectively subtracts away the diffuse cloud in which the core is enveloped. As is clear in Figure 7*a*, there is no positive correlation between a core's mass and its line width, as would be expected if the cores are in a state of virial equilibrium. As was the case for the line width–size relation, the scatter in this diagram might suggest that mass and line width are negatively correlated, since larger line widths are more frequently observed for less massive ($<1\ M_\odot$) cores. But such an inference is due primarily to outliers, as our linear fit shows no correlation.

It may not be reasonable to assume that the line width at the extinction peak should correlate with core mass. The $C^{18}O$ beam traces the entire column density along the line of sight, which would include any contribution from the intercore material whose mass is not reflected in Figure 7*a* due to the removal of the background by the wavelet analysis. Furthermore, for 75% of the Pipe cores, the $C^{18}O$ beam subtends less than 20% of the area of

TABLE 4
CORRELATION ANALYSIS

Δv vs.	Fit[a] a0	Fit[a] a1	r_c[b]
v_{lsr}	0.21	0.05	0.24
log r(pc)	0.43	0.02	−0.17
log M_{core}	0.40	0.01	−0.15
log M_{beam}	0.47	0.25	0.08

[a] Result of linear least-absolute-deviation fit; a1 is the slope of the fit.
[b] Correlation coefficient.

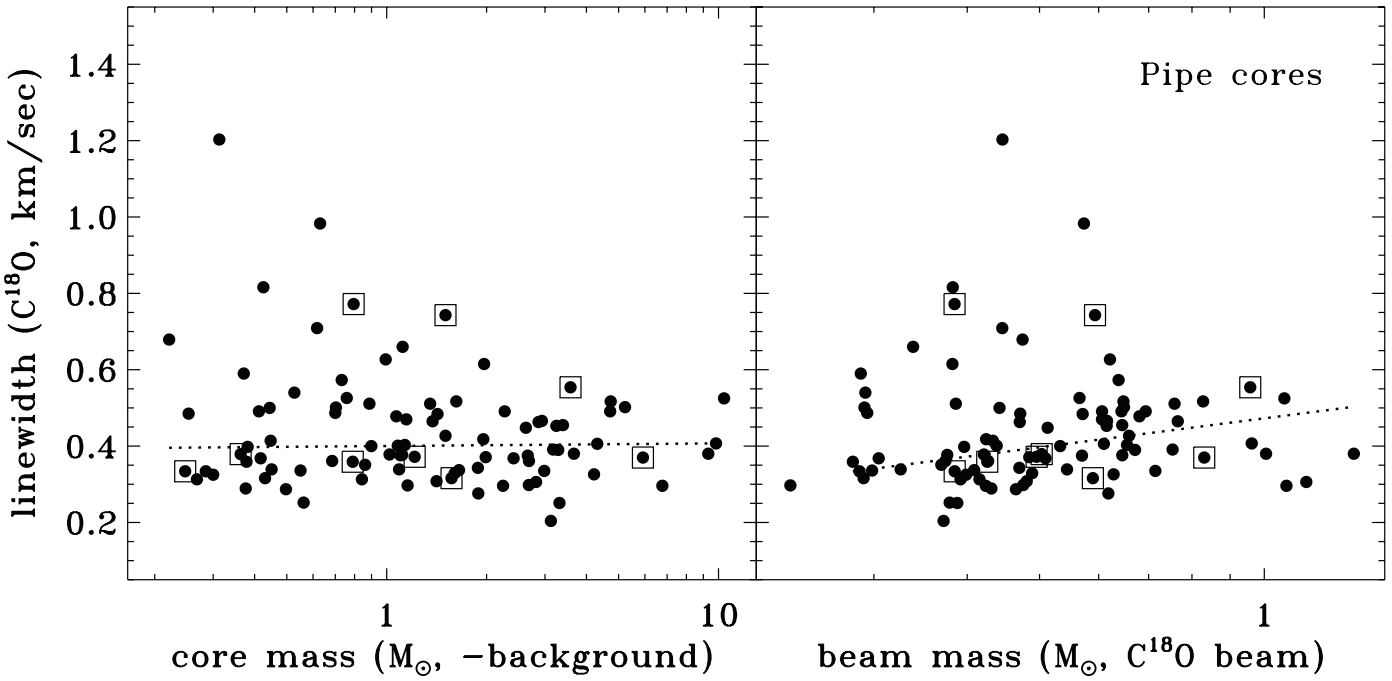

FIG. 7.—Core line width–mass relations for the Pipe. *Left*: Line width is plotted as a function of core mass, derived from the wavelet-subtracted map of Alves et al. (2007) and tabulated in Lada et al. (2007). *Right*: Line width is plotted as a function of the integrated column density seen by the radio beam, and expressed in mass units. Beam fluxes are given in Table 2. Circles surrounded by squares represent the "a" component of extinction cores with two C^{18}O components. A least-absolute-deviation fit is shown (Table 4).

the extinction core. Perhaps it is more precise to ask if the line width correlates with the observed column density in the AR012m beam (56″) as determined from the 2MASS/NICER extinction map without subtracting for background. Using `wphot` in IRAF, we measured the total flux expressed in A_V within a Gaussian-weighted beam with a 56″ FWHM and summed to 3 σ ($R = 71''$). Table 2 is supplemented with these fluxes. In Figure 7*b*, we convert this flux to mass[8] and compare it to the line width. A linear fit suggests that line width is more correlated to central beam mass than core mass. This could suggest that extinction cores that find themselves embedded in larger cloud envelopes have slightly larger line widths than cores that are isolated. Because ammonia observations that trace higher density gas confirm the lack of line width variations with the cores' sizes (Rathborne et al. 2007), we instead believe that our C^{18}O data are picking up non-negligible emission from intercore gas.

4. DISCUSSION

4.1. *Large-Scale Kinematics of the Pipe Nebula*

In this section, we examine the large-scale kinematics of the Pipe nebula. As was clear in Figure 3, the dense extinction cores in the molecular cloud display strong spatial $v_{\rm lsr}$ variations. The $v_{\rm lsr}$ distribution function (Fig. 8) of these cores allows us to broadly characterize the Pipe nebula's *dense* core kinematics, which appear to consist of two components. Fitting these components as Gaussian distributions yields central velocities of $v_{\rm lsr,1} = 3.48$ and $v_{\rm lsr,2} = 4.95$ km s^{-1}, with corresponding dispersions of $\sigma(v_1) = 0.37$ and $\sigma(v_2) = 0.55$ km s^{-1}.

[8] The conversion from total column density as measured in magnitudes of extinction (A_V) is 0.00757 $M_\odot$ mag^{-1}. This constant is derived assuming a distance of 130 pc (Lombardi et al. 2006), using a size of 30″ pixel^{-1} in the extinction map, and employing the basic atomic and astrophysical constants as given by Cox (2000).

Using the $v_{\rm lsr}$ distribution function for the dense extinction cores as a guide, the global kinematic structure of the Pipe cloud becomes very evident in the ^{13}CO channel maps of Onishi et al. (1999). Overlaying two channel maps centered at 3.5 and 5 km s^{-1} onto our extinction map in Figure 9, we show that these two components are clearly spatially organized: the primary component of the Pipe is a 15 pc long filament centered at $v_{\rm lsr} \sim 3.5$ km s^{-1} and stretching (7°) across our entire field of view. Surprisingly, this main component is narrow both physically and kinematically, especially in the Stem of the Pipe. As it twists around one side of the Bowl, the main component is somewhat redshifted ($v_{\rm lsr} \sim 4$ km s^{-1}) relative to the Stem, but shifts back to 3.5 km s^{-1} for $l > 1.5°$ (see also Fig. 3*a*). The molecular material of the 5 km s^{-1} component is concentrated in a coherent feature within the Bowl that parallels the slightly redshifted portion of the main component.

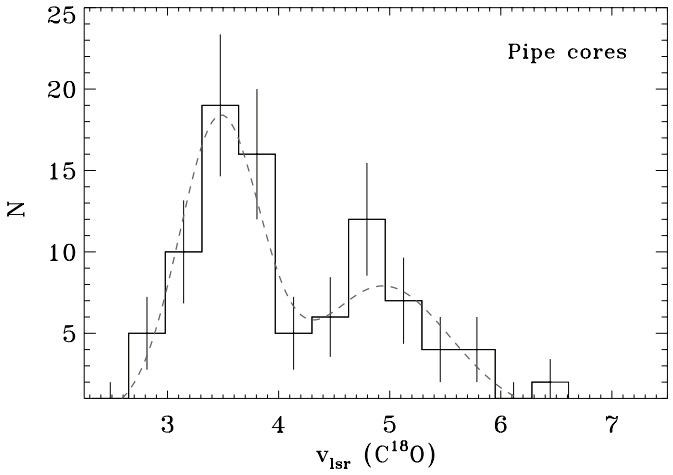

FIG. 8.—The $v_{\rm lsr}$ distribution function for the Pipe C^{18}O cores. A two-component Gaussian profile fit is shown; see text.

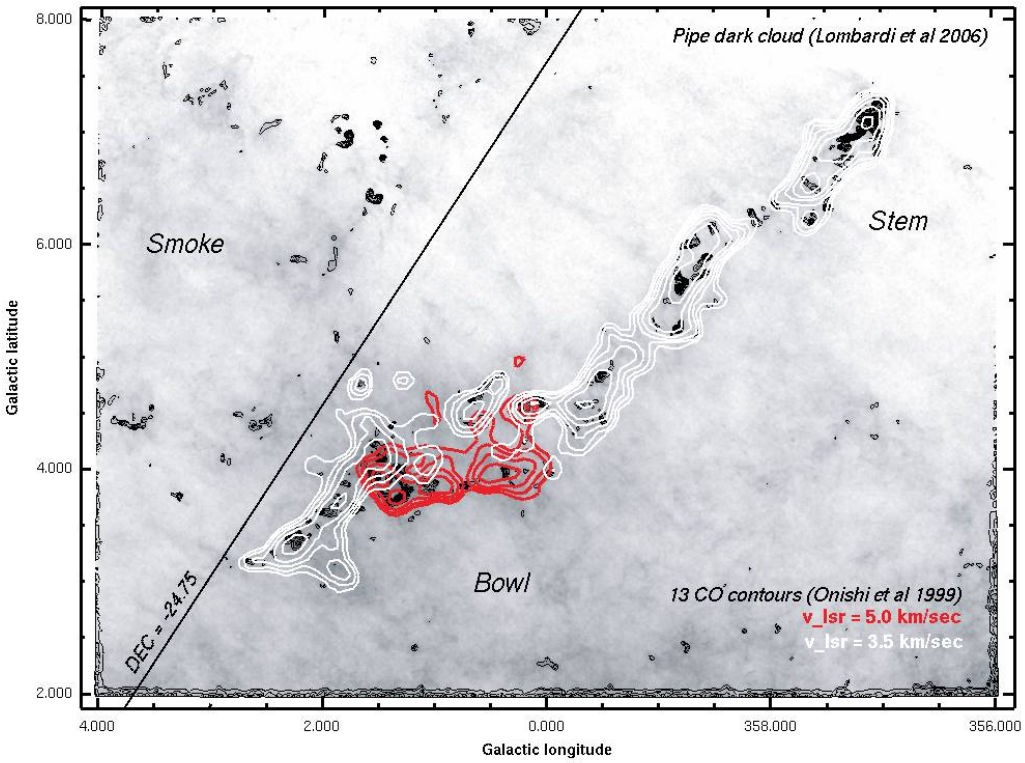

FIG. 9.— Smoothed ^{13}CO channel maps at 3.5 (*white contours*) and 5.0 (*red contours*) km s^{-1}, illustrating the two primary velocity components of the Pipe nebula (data from Onishi et al. 1999). These components trace the large-scale kinematic feature we refer to as the Pipe molecular ring. Black contours correspond to the wavelet-subtracted map of Alves et al. (2007), overplotted on the complete 2MASS extinction map (*inverted gray-scale*). This figure was created using SAOImage DS9 (Joye & Mandel 2003).

It overlaps the 3.5 km s^{-1} component at $l = 0^\circ$ and $l = 1.5^\circ$, forming an apparent "ring" in the Bowl. We now explore more closely the kinematics of each portion of the Pipe.

4.1.1. *Kinematics of the Stem*

As is clear in Figure 5, the Stem of the Pipe displays a very different kinematic signature than the Bowl; specifically, the extinction cores in the Stem display smaller dispersions in *both* line width and $v_{\rm lsr}$. The Stem consists of a single well-organized, very linear structure. For Stem cores with C^{18}O data, we can fit the $v_{\rm lsr}$ distribution function with a single component, which is narrower even than the 3.5 km s^{-1} component fit in Figure 8. Over its 10 pc length, the dense cores in the Stem display a core-to-core standard deviation, $\sigma(v_{\rm lsr})$, of only 0.27 km s^{-1}. On the one hand, the core-to-core motions in the Stem are slightly larger than the sound speed (0.2 km s^{-1} at 10 K).[9] On the other hand, the gas contained within the Stem cores is subsonic; the median one-dimensional C^{18}O velocity dispersion for the gas within a dark extinction core in the Stem is $\sigma_{\rm 1D} = 0.16$ km s^{-1} ($\Delta v = 0.38$ km s^{-1}), with a variance of 1.3×10^{-3}. Summing these gas motions, i.e., $\sigma(v_{\rm lsr})$ and $\sigma_{\rm 1D}$, in quadrature, we derive a total one-dimensional velocity dispersion for C^{18}O in the Stem of 0.32 km s^{-1}, or 0.56 km s^{-1} in three dimensions ($\sigma_{\rm 3D}$). Again, this is not much larger than the three-dimensional sound speed of molecular hydrogen (0.35 km s^{-1}). Moreover, it is significantly smaller than those values typical for 10 pc structures as derived by Larson (1981). Those structures display $\sigma_{\rm 3D} \sim 2.5$ km s^{-1}.

[9] Rathborne et al. (2007) found a typical kinetic temperature of 12 ± 2 K using ammonia measurements of a sample of these Pipe cores.

Larson commented that on these (10 pc) physical scales, large-scale $v_{\rm lsr}$ gradients contribute significantly to $\sigma_{\rm 3D}$. By eye, any gradient of $v_{\rm lsr}$ with Galactic longitude (Fig. 3*a*) appears quite small; a linear fit yields a gradient of $|\delta v_{\rm lsr}| \sim 0.1 \pm 0.1$ km s^{-1} deg^{-1}. The bulk motion of the gas along the Stem appears much more organized than in those clouds described by Larson. An alternate source for such a missing and substantially larger nonthermal component could be the lower density core and cloud envelopes. Our analysis of C^{18}O on different size scales (§ 3.3.1) suggests that any "additional" nonthermal line width can only be on an order of the typical line width, raising $\sigma_{\rm 3D}$ insignificantly. To examine gas at large scales and lower densities, we summed the Onishi et al. ^{13}CO line over the Stem; this experiment yields a total ^{13}CO line width of $\sim$1 km s^{-1}, or $\sigma_{\rm 3D} \sim 0.7$ km s^{-1}. We conclude that our observations of the dark extinction cores in the Stem of the Pipe are tracing the dense portions of a cloud in a different physical state than characterized by clouds studied by Larson.

4.1.2. *The Bowl and a Ring*

The Bowl is clearly composed of molecular gas from the two main velocity components, and it appears that these two velocity components trace a large coherent ringlike (in projection) structure of molecular material in the Bowl. We believe that the Pipe molecular ring is not a shell, because there are neither dense extinction cores nor significant ^{13}CO emission at any velocity at the center of the ring. Although the two components can be seen clearly in the ^{13}CO data cube of Onishi et al. (1999), the existence of multiple components in the Pipe was discussed only briefly by Onishi et al., who noted three C^{18}O cores at the eastern end of the ring that overlapped spatially, but had differing values of $v_{\rm lsr}$.

TABLE 5

REGIONAL CLOUD AND CORE EXTINCTION PROPERTIES

	CLOUD[a]			CORES[b]		
REGION	N_{pixels}	Total Flux (ΣA_V; mag)	Mass ($M/M_\odot$)	N_{cores}	ΣM_{total} ($M/M_\odot$)	ΣM_{bcksb} ($M/M_\odot$)
Stem	68621	196012	1500	53	208	102
Bowl	83498	410748	3100	57	308	95
Ring[c]	24519	147437	1100	37	230	70
Smoke	146272	367895	2800	49	106	47

[a] Cloud extinction properties derived from total extinction map of Lombardi et al. (2006) without subtraction for background. One pixel has an angular size of 30″. Although the regions are not circular, an effective radius for each region can be calculated as $0.01(N_{pixels})^{1/2}$ pc, assuming a distance of 130 pc (Lombardi et al. 2006).

[b] Core masses derived by summing individual extinction core masses as listed in Alves et al. (2007) without subtraction for the background cloud (ΣM_{total}) and after wavelet subtraction of the background (ΣM_{bcksb}; Lada et al. 2007).

[c] Note that the ring region is enclosed by the Bowl.

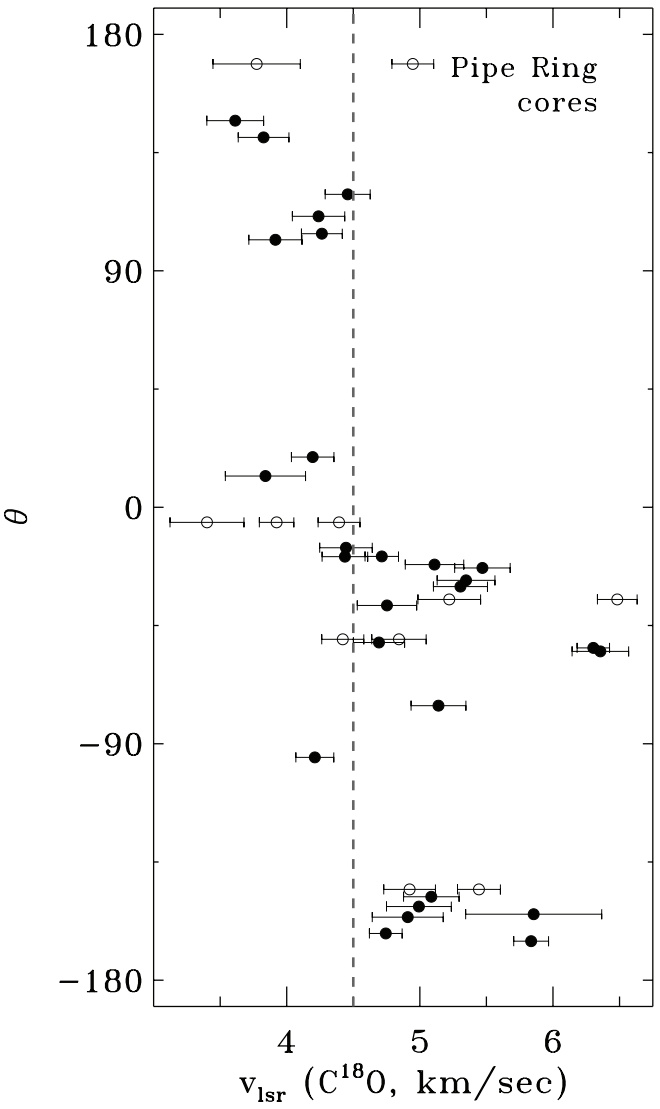

FIG. 10.— Variations in radial velocity within the Pipe molecular ring as traced by the C^{18}O data of the dark extinction cores (*circles*). Open circles correspond to cores with multiple C^{18}O components; the v_{lsr} of each component is shown. The 1 σ dispersion in C^{18}O is overplotted for each point. The dashed line at $v_{lsr} = 4.5$ km s^{-1} corresponds approximately to that velocity at which emission from ^{13}CO can be seen around the entire ring. The projection onto polar coordinates was performed centering on $(l, b)_0 = (0.755^\circ, 4.172^\circ)$. The axis of increasing Galactic longitude (east) corresponds to 0°; 90° is increasing Galactic latitude (north); 180° corresponds to where the base of the Stem and the ring meet (west, $l \sim 0^\circ$).

At $v_{lsr} = 4.5$ km s^{-1}, the Pipe molecular ring forms a projected ellipse in ^{13}CO, with maximum spatial dimensions of 4.7×2.9 pc and an effective radius $[(\text{area}/\pi)^{1/2}]$ of 2.1 pc. Its total mass is $\sim$1100 $M_\odot$ (Table 5), which was calculated from the Lombardi et al. (2006) 2MASS extinction map, and excludes the flux of the central hole, with a radius of $\sim$1 pc and a mass of 150 $M_\odot$. Alves et al. identified 37 dark extinction cores in this ring; these dense cores comprise $\sim$6% of the total ring mass. We observed 32 of them in C^{18}O.

The ballistics of the dense extinction cores as determined from our C^{18}O observations permit us to further investigate the nature of this ring. Taken as an ensemble, the maximum radial velocity difference for the ring cores is 2.2 km s^{-1}, with $\sigma(v_{lsr}) = 0.61$ km s^{-1}. These core-to-core motions are (very) large relative to the motions of cores in the Stem (Fig. 3), and are due at least in part to the systematic nature of the v_{lsr} variations around the ring. These core motions are not, however, sufficient to allow them to escape the gravitational field of the Ring ($v_{esc} \sim 2.35$ km s^{-1}). After projecting the locations of the cores into polar coordinates,[10] we plot the values of v_{lsr} versus angle, θ, which places us in the reference frame of the ring, and angularly traces the ring's circumference (Fig. 10).[11] First, we can see that the dense cores are not behaving as a rotating ring, which would trace a parabola in this figure. There are instead strong gradients in v_{lsr} at $\theta = 0^\circ$ and $\theta = -180^\circ$. The cores in the northern half of the ring ($\theta > 0$) are only somewhat redshifted relative to the main cloud ($v_{lsr} = 4$ km s^{-1}), while their localized core-to-core motions are similar to the Stem [$\sigma(v_{lsr}) \sim 0.27$ km s^{-1}; Table 6].

[10] Projection centered at $(l, b)_0 = (0.755^\circ, 4.172^\circ)$.

[11] The value $\theta = 0^\circ$ corresponds to increasing Galactic longitude (east); 90° is increasing Galactic latitude (north); ±180° corresponds to where the base of the Stem and the ring meet (west, $l \sim 0^\circ$).

TABLE 6

RING C^{18}O PROPERTIES

Quadrant	N_{cores}	$\langle v_{lsr} \rangle$	$\sigma(v_{lsr})$	$\langle \sigma_{1d} \rangle$
180° → 90°	6	4.05	0.29	0.19
90° → 0°	2	4.02	0.18	0.23
0° → −90°	12	5.17	0.61	0.20
−90° → −180°	7	5.09	0.54	0.23
North	8	4.04	0.27	0.20
South	19	5.14	0.59	0.21

NOTE.—All velocity dispersions are given in units of km s^{-1}.

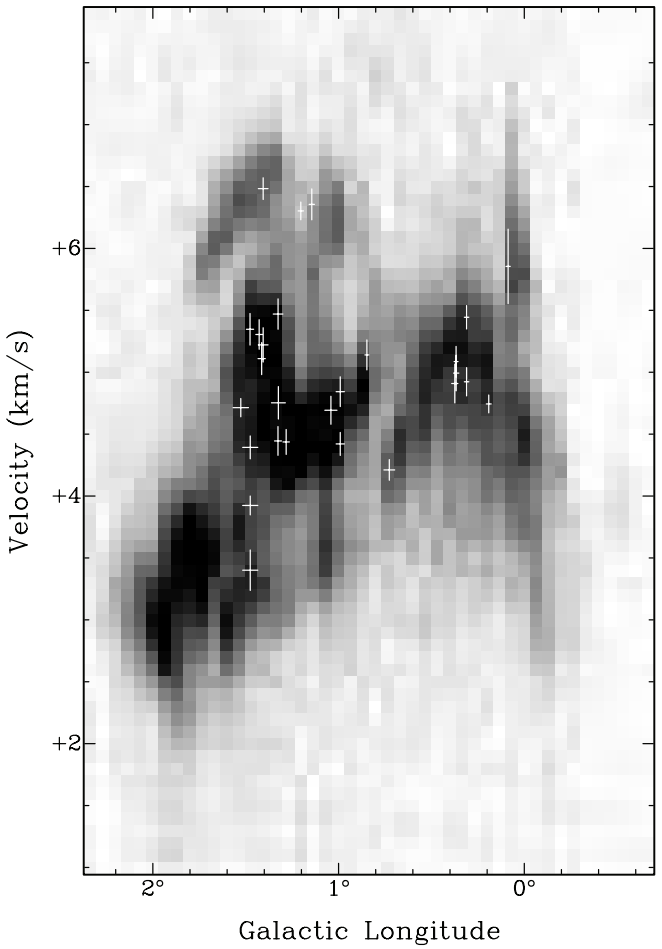

FIG. 11.—Variations in radial velocity along the Pipe molecular ring traced using the ^{13}CO data of Onishi et al. (1999). This figure is the ^{13}CO Galactic longitude-velocity diagram (l, v) averaged over a 0.6° band centered at $b = 3.9°$. It corresponds to the ^{13}CO gas enveloping those cores with negative values of θ in Fig. 10. The extinction cores in this part of the ring are overplotted as crosses, using their C^{18}O v_{lsr}. The crosses have widths in l, v corresponding to the extinction core's radius and C^{18}O line width.

The extinction cores in the southern half of the ring are clearly centered on the 5 km s^{-1} cloud component. However, they display radial velocity variations [$\sigma(v_{lsr}) \sim 0.6$ km s^{-1}] that do not appear to be related to the overall ring structure, and are much larger than in the northern half. To better illustrate these motions, we plot in Figure 11 a ^{13}CO position-velocity diagram aligned with this part of the ring ($\theta < 0°$). Note that this l-v diagram is integrated over a 0.6° wide band centered at approximately $b = 3.9°$. In ^{13}CO, we observe a rapid but systematic transition from the 3.5 km s^{-1} to the 5 km s^{-1} clouds at $l = 1.5°$. Along the extent of the 5 km s^{-1} component, we observe large variations in the lower density gas, ranging from 4 to 6.5 km s^{-1}, and mirrored by the kinematics of the denser cores. In addition to cores at 5 km s^{-1}, there appears to be gas with dense cores clustered at 6.3 km s^{-1}, as well as at least one core at 4 km s^{-1}.

When we perform the same experiment for the Pipe molecular ring as for the Stem, and average the ^{13}CO data for the Bowl, we find $\sigma_{3D} \sim 1.8$ km s^{-1}, substantially larger than the Stem. As we have shown, most of this dispersion comes from the systematic velocity difference between the two components ($\Delta v_{lsr} = 1$ km s^{-1}) and from the larger core-to-core motions in the ring [$\sigma(v_{lsr}) \sim 0.6$ km s^{-1}]. Yet it is also important to notice that cores all around the ring display line widths that are elevated (0.48 km s^{-1}) relative to the Stem (0.38 km s^{-1}) or any other part of the Pipe cloud (Table 6).

It is not clear whether the ring is a single coherent feature or a superposition of two independent filaments, one of which (the ~5 km s^{-1} portion) is substantially clumpier than the other. We can say that the extinction cores in the northern portion of the ring differ from the main 3.5 km s^{-1} cloud in that they are redshifted slightly and display slightly larger line widths. Even if these facts point to a physical association for the two sides of the ring, we cannot infer the line-of-sight geometry for this complicated region, and cannot precisely ascertain an origin for these kinematics. The net velocity difference ($\Delta v_{lsr} \sim 1$ km s^{-1}) between the two sides of the ring may be the signature of either a collapse or an expansion, although it does constrain the region's evolutionary timescale to be of order 2 Myr. Thus, either case could correspond to a primordial kinematic feature from the creation of the cloud. We prefer a primordial explanation, because the cores of the ring appear bound to it, and we think it unlikely that the cloud has been modified by some localized but external event. The kinetic energy of the ring is of order 10^{46} ergs, which is too small to suggest the influence of a nearby supernova. Such an event would likely have also similarly impacted a much larger portion of the cloud. Onishi et al. (1999) examined the possible influence of nearby B stars, finding them too distant to affect any portion of the Pipe except Barnard 59, which is ~5° away.

We can further compare the Pipe molecular ring[12] to physical structures found in the Taurus molecular cloud. There are two features in Taurus that have received attention as apparent rings: Heiles Cloud 2 (HCl2; Schloerb & Snell 1984; Cernicharo & Guelin 1987) and Barnard 18 (Murphy & Myers 1985). Both clouds have masses (10^3 $M_\odot$), radii (1–2 pc) and internal velocity differences (1–2 km s^{-1}) similar to the Pipe. HCl2 has an obvious ringlike structure in the extinction map of Padoan et al. (2002; see also Tóth et al. 2004), while Barnard 18 is primarily a weak kinematic structure without strong CO or extinction signatures. Moreover, the kinematics of HCl2 are much more similar to those we find in the Pipe molecular ring, displaying complicated signatures of overlapping filaments that do not trace a rotating ring (Cernicharo & Guelin 1987).

To speculate on an origin for such structures, it is important to recognize a fundamental difference between the Pipe and Taurus, namely the present-day star formation rate. The Taurus cloud likely represents a more evolved star-forming analog to the Pipe nebula; indeed, both of the rings in Taurus contain young stars. In fact, Murphy & Myers suggested that Barnard 18 is an expanding ring caused by a small group of ~10 stars projected near its center (Myers 1982). As illustrated by Tóth et al. (2004), the HCl2 ring contains star formation on at least two sides, including a Class I protostar in TMC-1 and *IRAS* point sources in IC 2087. The Pipe molecular ring is apparently free of any present-day star formation. Onishi et al. (1999) found no *IRAS* point sources within the Pipe molecular ring that have the colors of young stellar objects, and our visual inspection of *IRAS* scans and optical DSS plates indicate to us that there are *neither IRAS* sources of any color, nor bright DSS sources that could be B stars in this ring. Simply, there do not appear to be any young stars in or near the ring whose outflows would be responsible for its kinematics. We find that the existence of the Pipe molecular ring without young stars supports a hypothesis that such ringlike structures are likely primordial, resulting from the creation of the cloud.

[12] We so name this apparent feature to reflect its similarities to the Taurus molecular ring, a moniker given to HCl2 in the literature.

4.1.3. *The Smoke*

Most of the Smoke extinction cores we observed with $C^{18}O$ are in fact members of the 5 km s^{-1} component, although a full discussion of spatial variations in v_{lsr} in the Smoke is limited by our spatial incompleteness. Excluding three cores that are in the 3 km s^{-1} component, the remaining 9 $C^{18}O$ cores have $v_{lsr} = 4.8$ km s^{-1}, with $\sigma(v_{lsr}) = 0.2$ km s^{-1}, which is smaller even than the Stem. The extinction cores in the Smoke have uniformly narrow line widths, with a median $\Delta v = 0.4$ ($\sigma = 0.14$) km s^{-1}; their total $C^{18}O$ $\sigma_{3D} = 0.4$ km s^{-1}, with similar spatial dimensions as the Stem, albeit with a different projected geometry. As was the case for the Bowl, the Alves et al. (2007) cores constitute only 2% of the total column density in the Smoke (Table 5). Indeed, most of the mass for the Smoke is in very diffuse gas; 2/3 of the total Smoke mass is in regions with $A_V < 2$ mag. Interestingly, there is no core in the Smoke with a mass greater than 2 $M_\odot$.

A discussion of a few of the Smoke extinction cores is warranted. Barnard 68 (Pipe-101) and Barnard 72 (aka "the Snake," Pipe-111, Pipe-112, and GF 1; Schneider & Elmegreen 1979) can be seen at $l = 2^\circ, b = 7^\circ$ in Figures 3 and 9. These dark extinction cores have a striking, dark appearance at optical wavelengths, which has led to their frequent appearance in astrophotographs. These cores are separated angularly by about 17′, but they are separated in velocity by 1.5 km s^{-1} (3.36 vs. 4.96 km s^{-1}). Further observations will be valuable to determine how the velocities of cores in the Pipe's Smoke are spatially distributed.

5. CONCLUSIONS

We have used the ARO 12 m radio telescope to characterize the molecular gas properties of the dark extinction cores identified by Alves et al. (2007) in the near-IR extinction map derived by Lombardi et al. (2006). We obtained central pointings for 94 dark extinction cores in the $C^{18}O$ $J = 1$–0 line at an angular resolution optimally matched to the resolution of the extinction map. All the cores were detected in $C^{18}O$, and less than 10% of the cores display multiple velocity components. This confirms that most of the extinction cores in the Pipe are true dense cores, and are not the superposition of unrelated filaments. We find no correlations between the derived molecular line widths of $C^{18}O$ and the properties (R, M) of these dark extinction cores. These noncorrelations are confirmed by higher density ammonia observations (Rathborne et al. 2007), and interpreted by Lada et al. (2007) as evidence that the cores of the Pipe are thermally supported and in pressure equilibrium with the external cloud.

While we find no correlation between basic core properties and the molecular $C^{18}O$ line width, we do find a strong correlation between a Pipe extinction core's radial velocity and its location in the cloud. We find that there are two well-defined velocity components of the molecular gas in the Pipe. One is primarily located in a very narrow spatial feature that stretches 15 pc across the region, and is characterized by a small dispersion in radial velocity. Its internal kinematics and gas motions are inconsistent with the relations derived by Larson (1981) for large turbulent gas clouds. The second component forms half of an apparent ring within the Bowl of the Pipe, with a radius of ~2 pc and a mass of ~1000 $M_\odot$. The extinction cores in the Pipe molecular ring have line widths somewhat elevated relative to those cores in the main cloud component. The lower density ^{13}CO gas displays far larger motions than similar gas of the main component. Unlike similar rings in Taurus, there are no apparent young stars in the Pipe molecular ring that could be modifying the cloud cores' kinematics. Thus, both the Stem of the Pipe and the Pipe molecular ring appear to be primordial features of this young dark cloud. In summary, we find the kinematics of the Pipe cloud to be relatively quiescent over most of its 15 pc length, having subsonic $C^{18}O$ extinction cores and displaying core-to-core motions only somewhat larger than the gas sound speed. The mostly systematic nature of motion in the Pipe molecular ring warrants further detailed study through spatially complete mapping of $C^{18}O$, as well as molecular line transitions that trace higher densities.

We extend our appreciation to the staff of the Arizona Radio Observatory (ARO) for supporting our observations and scheduling ample observing time. The Kitt Peak 12 m is operated by the Arizona Radio Observatory, Steward Observatory, and the University of Arizona. We further thank T. Onishi for access to the ^{13}CO cube of the Pipe. An anonymous referee provided comments that improved parts of this paper. This research made use of IDL procedures developed by and publicly available from C. Markwardt. This research made use of SAOImage DS9, developed by the Smithsonian Astrophysical Observatory (Joye & Mandel 2003). This research was supported in part by NASA Origins grant NAG10341 and a NASA *Spitzer* grant.

Facilities: ARO:12m

REFERENCES

Alves, J. F., Lada, C. J., & Lada, E. A. 2001, Nature, 409, 159
Alves, J., Lombardi, M., & Lada, C. J. 2007, A&A, 462, L17
Barnard, E. E., Frost, E. B., & Calvert, M. R. 1927, A Photographic Atlas of Selected Regions of the Milky Way (Washington: Carnegie Inst.)
Brooke, T. Y., et al. 2007, ApJ, 655, 364
Cambrésy, L. 1999, A&A, 345, 965
Cernicharo, J., & Guelin, M. 1987, A&A, 176, 299
Cox, A. N. 2000, Allen's Astrophysical Quantities (4th ed.; New York: AIP)
Dobashi, K., Uehara, H., Kandori, R., Sakurai, T., Kaiden, M., Umemoto, T., & Sato, F. 2005, PASJ, 57, 1
Joye, W. A., & Mandel, E. 2003, in ASP Conf. Ser. 295, Astronomical Data Analysis Software and Systems XII, ed. H. E. Payne, R. I. Jedrzejewski, & R. N. Hook (San Francisco: ASP), 489
Kutner, M. L., & Ulich, B. L. 1981, ApJ, 250, 341
Lada, C. J., Lada, E. A., Clemens, D. P., & Bally, J. 1994, ApJ, 429, 694
Lada, C. J., Muench, A. A., Rathborne, J., Alves, J. F., & Lombardi, M. 2007, ApJ, submitted (arXiv:0709.1164)
Larson, R. B. 1981, MNRAS, 194, 809
Lee, C. W., & Myers, P. C. 1999, ApJS, 123, 233
Lee, C. W., Myers, P. C., & Tafalla, M. 1999, ApJ, 526, 788
———. 2001, ApJS, 136, 703
Lombardi, M., & Alves, J. 2001, A&A, 377, 1023
Lombardi, M., Alves, J., & Lada, C. J. 2006, A&A, 454, 781
Motte, F., Andre, P., & Neri, R. 1998, A&A, 336, 150
Murphy, D. C., & Myers, P. C. 1985, ApJ, 298, 818
Myers, P. C. 1982, ApJ, 257, 620
Onishi, T., et al. 1999, PASJ, 51, 871
Padoan, P., Cambrésy, L., & Langer, W. 2002, ApJ, 580, L57
Rathborne, J., Lada, C. J., Muench, A. A., Alves, J. F., & Lombardi, M. 2007, ApJS, submitted (arXiv0708.3660)
Reipurth, B., Nyman, L.-A., & Chini, R. 1996, A&A, 314, 258
Schloerb, F. P., & Snell, R. L. 1984, ApJ, 283, 129
Schneider, S., & Elmegreen, B. G. 1979, ApJS, 41, 87
Tachihara, K., Mizuno, A., & Fukui, Y. 2000, ApJ, 528, 817
Tóth, L. V., Haas, M., Lemke, D., Mattila, K., & Onishi, T. 2004, A&A, 420, 533
Williams, J. P., de Geus, E. J., & Blitz, L. 1994, ApJ, 428, 693
Wolf, M. 1923, Astron. Nachr., 219, 109